Highlights:

- 4D quantification of growing clinopyroxene and plagioclase crystals
- Temperature and time control the nucleation of pyroxene and plagioclase in basalts
- Investigation of the crystal effect on the rheology and transport of basaltic lava
- Reproduction of the final solidification history of the 2001 Etna lavas
- Application of real-time synchrotron X-ray imaging to forecast lava flow hazards

1   *In situ* quantification of crystallisation kinetics of plagioclase and

2   clinopyroxene in basaltic magma: implications for lava flow

3

4   **Nolwenn Le Gall[1,2]*, Fabio Arzilli[3], Giuseppe La Spina[3], Margherita Polacci[3], Biao Cai[4],**

5   **Margaret E. Hartley[3], Nghia T. Vo[5], Robert C. Atwood[5], Danilo Di Genova[6], Sara**

6   **Nonni[7], Edward W. Llewellin[8], Mike R. Burton[3], Peter D. Lee[1,2]**

7

8   [1]Department of Mechanical Engineering, University College London, London, WC1E 7JE,

9   UK

10   [2]Research Complex at Harwell, Rutherford Appleton Laboratory, Harwell, Oxfordshire,

11   OX11 0FA, UK

12   [3]Department of Earth and Environmental Sciences, University of Manchester, Manchester,

13   M13 9PL, UK

14   [4]School of Metallurgy and Materials, University of Birmingham, Birmingham, B15 2TT, UK

15   [5]Diamond Light Source Ltd., Didcot, OX11 0DE, UK

16   [6]Bayerisches Geoinstitut, Universität Bayreuth, 95440 Bayreuth, Germany

17   [7]University of Manchester at Harwell, Didcot, OX11 0DE, UK

18   [8]Department of Earth Sciences, Durham University, Durham, DH1 3LE, UK

19   *n.gall@ucl.ac.uk

20

Abstract

21

22 Crystallisation is a complex process that significantly affects the rheology of magma, and

23 thus the flow dynamics during a volcanic eruption. For example, the evolution of crystal

24 fraction, size and shape has a strong impact on the surface crust formation of a lava flow, and

25 accessing such information is essential for accurate modelling of lava flow dynamics. To

26 investigate the role of crystallisation kinetics on lava flow behaviour, we performed real-

27 time, *in situ* synchrotron X-ray microtomography, studying the influence of temperature-time

28 paths on the nucleation and growth of clinopyroxene and plagioclase in an oxidised,

29 nominally anhydrous basaltic magma. Crystallisation experiments were performed at

30 atmospheric pressure in air and temperatures from 1250 °C to 1100 °C, using a bespoke high-

31 temperature resistance furnace. Depending on the cooling regime (single step *versus*

32 continuous), two different crystal phases (either clinopyroxene or plagioclase) were

33 produced, and we quantified their growth from both global and individual 3D texture

34 analyses. The textural evolution of charges suggests that suppression of crystal nucleation is

35 due to changes in the melt composition with increasing undercooling and time. Using

36 existing viscosity models, we inferred the effect of crystals on the viscosity evolution of our

37 crystal-bearing samples to trace changes in rheological behaviour during lava emplacement.

38 We observe that under continuous cooling, both the onsets of the pāhoehoe-ʻaʻā transition

39 and of non-Newtonian behaviour occur within a shorter time frame. With varying both

40 temperature and time, we also either reproduced or approached the clinopyroxene and

41 plagioclase phenocryst abundances and compositions of the Etna lava used as starting

42 material, demonstrating that real-time synchrotron X-ray tomography is an ideal approach to

43 unravel the final solidification history of basaltic lavas. This imaging technology has indeed

44 the potential to provide input into lava flow models and hence our ability to forecast volcanic

45 hazards.

46

49

1. Introduction

Nucleation and growth of crystals are complex processes that dramatically affect the evolution of textures in cooling magmas, and therefore the eruptive dynamics. These processes have been extensively studied, but mainly *ex situ* using laboratory cooling and decompression experiments (e.g. Mollo and Hammer, 2017, for a review; Giuliani et al., 2020, and references therein) and through the textural analysis of both experimental and eruptive products from two-dimensional (2D) and three-dimensional (3D) methods (e.g. Baker et al., 2012, and references therein). Until very recently, there was a paucity of *in situ* data (Ni et al., 2014; Schiavi et al., 2009). Thanks to the emerging developments of X-ray synchrotron imaging techniques and *in situ* apparatus (e.g. Azeem et al., 2017; Drakopoulos et al., 2015), we can now directly capture the progressive development of a crystal texture in 4D (Arzilli et al., 2019; Polacci et al., 2018; Tripoli et al., 2019), i.e. three spatial dimensions plus time, which provides a deeper understanding of magma crystallisation and solidification during flow emplacement.

Pāhoehoe and ʻaʻā are the two most common surface morphologies in basaltic lava flows, with smooth and rough textures, respectively (e.g. Wentworth and Macdonald, 1953; Peterson and Tilling, 1980). Most lavas initially erupt as pāhoehoe and may evolve to ʻaʻā during the progress of the flow. This irreversible transition (e.g. Hon et al., 2003) occurs dominantly in response to the increase in viscosity that, in turn, is controlled by the chemical

3

69 evolution of the residual melt, oxygen fugacity conditions and the increase in crystallinity

70 with distance from the vent (e.g. Cashman et al., 1999; Peterson and Tilling, 1980; Vona et

71 al., 2011). Thus, pāhoehoe lavas are typically less crystalline (<25–30 vol% vs >35 vol%)

72 and less viscous than ʻaʻā lavas.

73 Here, we studied and quantified *in situ* the nucleation and growth kinetics of pyroxene and

74 plagioclase, the two most common phenocrysts in basaltic magmas. These phenocrysts were

75 produced during single-step and continuous cooling experiments, to evaluate the effect of

76 varying both temperature and time on crystal texture. Specifically, we monitored the

77 evolution of the volume fraction, size and shape of clinopyroxene and plagioclase

78 phenocrysts. We also determined the rheology of the crystal-bearing samples for an accurate

79 modelling of lava flow behaviour. Polacci et al. (2018) and Arzilli et al. (2019) partially

80 presented the single-step cooling experiments. Polacci et al. (2018) quantified the

81 disequilibrium crystallisation of clinopyroxene and titanomagnetite using an empirical model

82 accounting for the volume fraction of crystals, while Arzillli et al. (2019) show that rapid (in

83 minutes) crystallisation can trigger magma fragmentation in highly explosive basaltic

84 eruptions. In this work, we present new data that enables us to (1) quantify the 3D growth of

85 individual clinopyroxenes and plagioclases, (2) infer the evolving rheology of the crystal-

86 bearing samples, and (3) compare the crystallisation kinetics induced under different cooling

87 pathways. As such, this work contributes to a better understanding of the final solidification

88 history of lava flows at basaltic volcanoes.

89

90 **2. Material and Methods**

91 2.1. *Starting material*

92   A sample suite from the Lower Vents (LV, 2500 m and 2100 m vents) of the 2001 eruption

93   of Mt. Etna, Italy (ET01, Table 1), was used as the starting material for the *in situ* cooling

94   experiments. The erupted trachybasaltic lava (47.7 wt% SiO_2, 5.3 wt% Na_2O+K_2O, Corsaro

95   et al., 2007) contains phenocrysts of clinopyroxene (8–14 vol%), plagioclase (4–7 vol%),

96   olivine (1–3 vol%) and titanomagnetite (less than 1 vol%). Most of the clinopyroxene

97   crystals are subhedral and sub-millimeter in size; others range from 3 to 10 mm. Plagioclase

98   crystals are euhedral and sub-millimeter in size; millimeter crystals are rare (Corsaro et al.,

99   2007).

100   The rock sample was crushed, placed in a platinum (Pt) crucible and melted in a 1 atm

101   Nabertherm $MoSi_2$ box furnace at 1400 °C for 4 h in air. The process was repeated twice. The

102   melt was then quenched by pouring it onto a steel plate, before being cored into glass

103   cylinders measuring 2.8 mm in diameter $\times$ 4 mm in length. The composition of the anhydrous

104   starting glass was measured by Electron probe microanalysis (EPMA) (Table 1).

105

106   2.2. *Experimental approach*

107   Two types of cooling-driven crystallisation experiments were carried out, defined by either

108   (1) a large drop in temperature followed by a dwell time of 4 h at the target temperature

109   (*single-step cooling* SSC) or (2) a continuous temperature decrease at a constant rate

110   (*continuous cooling* CC). These experiments were performed at the I12 beamline of the

111   Diamond Light Source (DLS, Harwell campus, United Kingdom) using the Alice high

112   temperature (max 1460 °C) resistance furnace with controlled heating/cooling rate (max 24

113   °C/min; Azeem et al., 2017). The cylindrical samples were contained in alumina (Al_2O_3)

114   holders (inner diameter 3 mm, wall thickness 0.5 mm) that were fitted on top of an Al_2O_3 rod

115   attached to the rotation stage, as shown in the sketch in Fig. 1. During the experiments, the

116 temperature was monitored to ± 5 °C by two type R thermocouples placed close to the

117 sample holder.

118 All experiments were performed in air, at ambient pressure and a temperature ranging

119 between 1100 °C and 1250 °C to simulate lava flows at near-vent conditions. The

120 experimental procedure (Fig. 2, Table 2) consisted of an initial constant heating (at 24

121 °C/min) of the sample up to 1250 °C, which is above the liquidus temperature, and a 30 min

122 isothermal hold to ensure the sample was completely melted and homogeneous. The sample

123 was then either cooled as rapidly as possible (24 °C/min) to 1170 °C (experiment SSC1170)

124 or 1150 °C (experiment SSC1150) and held at constant temperature for 4 h, or cooled at a

125 controlled rate of 0.5 °C/min to 1100 °C (experiment CC0.5), before cooling down to room

126 temperature (at 24 °C/min). The choice of a cooling rate of 0.5 °C/min is within the range of

127 estimated rates at which basaltic lava flows cool (0.01–15 °C/min, Cashman et al., 1999;

128 Witter and Harris, 2007).

129 During cooling-induced crystallisation, synchrotron X-ray tomography was conducted in

130 phase-contrast mode with a detector-sample distance of 2300 mm, in order to visualise and

131 analyse in real-time the nucleation and growth of crystals. X-ray tomographic images were

132 acquired using a 53 keV monochromatic X-ray beam and a high-speed camera, providing a

133 field of view of 8×7 mm^2 and a pixel size of 3.2 μm. In each scan dataset, a series of 1800

134 projections were acquired over a 180° rotation with an exposure time of 0.05 s per projection.

135 For each crystallisation experiment, up to 80 datasets were captured at a temporal resolution

136 of 3 min per scan, from before the end of sample melting/homogenisation at 1250 °C to the

137 final cooling down to room temperature.

138

139 2.3. *Analytical methods*

140 *2.3.1. Textural analysis*

141 Diamond Light Source in-house scripts derived from the Python-based framework TomoPy

142 (Gursoy et al., 2014) were used to reconstruct the tomographic datasets, including flat-field

143 correction, centre determination (Vo et al., 2014) and the removal of ring artefacts (Titarenko

144 et al., 2010) and blobs (Vo et al., 2018).

145 The reconstructed images were then processed using ImageJ (Abramoff et al., 2004, Fiji

146 Version 1.0) and Avizo (ThermoFisher Scientific, Version 9.4) software. ImageJ was first

147 used to reduce the size of the images to 8-bit, adjust brightness and contrast to highlight the

148 phenocrysts, and crop a Volume of Interest (VoI, 692×726×606–814 voxels) that contains

149 either clinopyroxene or plagioclase crystals. The VoI was chosen to exclude the top air/melt

150 interface meniscus and the trapped air bubbles at the bottom and edges of the sample

151 container (Fig. A.1a). All subsequent analysis was performed in Avizo (Fig. A.2). Noise

152 reduction was achieved by successively applying bilateral and median filters in 3D, in order

153 to efficiently segment crystals.

154 Crystals were segmented with interactive thresholding, and successively dilating, eroding

155 and/or opening the segmented volumes, as well as removing small particles (mainly oxides).

156 A large part of the oxides had to be removed manually due to the difficulty of automatically

157 identifying and separating them from the clinopyroxene and plagioclase phenocrysts. Three

158 scan datasets per experiment (9 in total) were selected, representing three different steps of

159 the crystallisation process at $t_1 = 60$ min, $t_2 = 160$ min and $t_3 = 200$ min after the start of the

160 dwell/cooling time (t_0).

161 In addition to quantify the mineral abundances (Table 2 and Fig. 3), a total of 10

162 clinopyroxenes in SSC1150 and 10 plagioclases in CC0.5 (Fig. A.3), located in various

163 places in the VoI, were isolated to measure their size (3D length L_{3D}) and volume (V), in

164   order to assess their growth rate in non-volumetric (Y_{L3D}) and volumetric (Y_V) terms (Figs. 4–

165   6, Tables 2, A.2 and A.3). Changes in crystal length/width aspect ratios (r_p) were also

166   quantified over time, with both the crystal length (Length3D) and width (Width3D)

167   automatically calculated as the longest and shortest Feret diameters, respectively. Most of the

168   segmented crystals were connected, corresponding to aggregates of single crystals (Polacci et

169   al., 2018), so no crystal number density is given.

170

171   *2.3.2. Chemical analysis*

172   Run products were analysed for their chemistry. Glass, titanomagnetite, clinopyroxene and

173   plagioclase crystals were analysed by EPMA using a Jeol JXA 8530F electron microprobe at

174   the University of Manchester, UK. Analyses were performed using a 15 kV accelerating

175   voltage, 10 nA beam current and beam size of 10 μ m. See Polacci et al. (2018) for more

176   details on the procedure.

177

178   **3. Results**

179   *3.1. Mineral assemblages and crystal abundances*

180   All experimental charges contain crystals of titanomagnetite (Table 2), confirming their

181   oxidised nature. They appeared visible in the melt after 12 and 6 min of the dwell time in the

182   SSC1170 and SSC1150 experiments (Polacci et al., 2018), respectively, and after 60 min of

183   continuous cooling in the CC0.5 experiment (although up to t_2 and reaching 1170 °C the

184   oxide volume fraction is near-zero). The two single-step cooled samples (SSC1170,

185   SSC1150) also contain clinopyroxene phenocrysts of augite composition (Table A.1), while

186   the continuously cooled sample (CC0.5) is characterised by the presence of plagioclase and

8

187   the absence of clinopyroxene. In both SSC1170 and SSC1150, plagioclase was not able to

188   form after 4 h at constant temperature. It started to grow only in the final cooling to room

189   temperature, at $T = 1131–1053$ °C for SSC1170 and $T = 1112–1073$ °C for SSC1150 (Arzilli

190   et al., 2019).

191   In SSC11170, the volume fraction of clinopyroxene is systematically very low (<0.002

192   vol%), with only three distinguishable crystals in the segmented VoI (Fig. 3a–c). They are

193   part of a small number of clinopyroxenes present at the bottom of the sample holder, which

194   appeared after 30 min of dwell time (Polacci et al., 2018) on the surface of an entrapped air

195   bubble and in close contact with alumina (Fig. A.1c). Since no other clinopyroxene crystals

196   nucleated in the rest of the charge within 4 h, the temperature of 1170 °C seems to be very

197   close to the liquidus temperature. Consequently, we defined the liquidus temperature of

198   clinopyroxene at 1170 °C.

199   In SSC1150, the nucleation of clinopyroxene crystals started within the first 12 min of the

200   dwell period (Polacci et al., 2018), preferentially at the air-melt interface and on alumina

201   walls (Fig. A.1b), i.e. heterogeneously. The clinopyroxene volume fraction increases with

202   time, from 1 vol% at $t_1 = 60$ min up to 9 vol% at $t_3 = 200$ min (Fig. 3d–f), as well as with

203   reducing temperature by 20 °C, from 1170 °C to 1150 °C (Fig. 3a–f).

204   In CC0.5, we did not observe any phenocryst crystallisation within the first hour of the

205   experiment. Plagioclase crystals started to nucleate and grow at ~1205 °C, i.e. after 90 min

206   from the beginning of cooling. They formed on tiny air bubbles attached to the walls of the

207   container. Afterwards, the volume fraction of plagioclase increased with increasing time and

208   decreasing temperature, reaching 22 vol% at $t_3 = 200$ min and $T = 1150$ °C (Fig. 3g–i).

209   Clinopyroxene crystallisation did not occur during the continuous cooling at 0.5 °C/min. A

210 few tiny crystals were observed in the final unquenched product, suggesting that they formed

211 somewhere during final cooling at 24 °C/min, at temperatures below 1100 °C.

212 In all three experiments, crystals nucleate mostly between t_1 and t_2 (Fig. 3) and then grow

213 with time and/or cooling, i.e. growth is dominant from t_2 onwards.

214

3.2. Crystal sizes and growth rates

216 Compared to previous studies, here we provide individual *in situ* 3D measurements of crystal

217 growth kinetics, contributing to a better understanding of crystallisation processes and, as a

218 consequence, of the solidification of basaltic lava flows.

219 Clinopyroxene size (L_{3D}) nearly triples with increasing the duration of the SSC1150

220 experiment, ranging from 90–320 μm at t_1 (60 min dwell) to 150–890 μm at t_2 (160 min

221 dwell) to 250–1090 μm at t_3 (200 min dwell, Fig. 4a, Tables 2 and A.2). Plagioclase L_{3D}

222 doubles with mutually increasing time and decreasing temperature in CC0.5, ranging from

223 270–520 μm at t_2 to 445–1160 μm at t_3 (Fig. 4b, Tables 2 and A.3). Both the clinopyroxene

224 and plagioclase volumes, averaged over 10 single crystals, increased fivefold from 0.3 to 1.6

225 $\times 10^{-6}$ cm^3 and from 0.8 to 3.8 $\times 10^{-6}$ cm^3, respectively, during the 140 min hold/cooling

226 from t_1 to t_3 (Fig. 4, Tables 2, A.2 and A.3). The average clinopyroxene growth rate (Y_{L3D}) is

227 nearly constant with time, ranging between 6.9 $\times 10^{-6}$ cm/s (t_1) and 5.8 $\times 10^{-6}$ cm/s (t_3), while

228 the average clinopyroxene volumetric growth rate (Y_V) almost triples between 4.6 $\times 10^{-11}$

229 cm^3/s (t_1) and 12 $\times 10^{-11}$ cm^3/s (t_3) (Fig. 5, Tables 2 and A.2). Both the average Y_{L3D} and Y_V

230 of plagioclase crystals are more impacted by time and temperature, with Y_{L3D} almost

231 quadrupling (3.7 to 16 $\times 10^{-6}$ cm/s) during 40 min of cooling from t_2 to t_3, and Y_V increasing

232 by a factor of 10 (4.1 to 55 $\times 10^{-11}$ cm^3/s, Fig. 5, Tables 2 and A.3).

233

3.3. Crystal morphologies

In SSC1150, clinopyroxene crystals formed with a gradual transition from elongated prismatic shapes to multi-branched crystals as growth proceeds (Fig. 4a; Polacci et al., 2018; Arzilli et al., 2019). Spherulitic morphologies were also observed, corresponding to heterogeneously nucleated crystal aggregates similar to that reported by Arzilli et al. (2015) for alkali feldspars. Plagioclase crystals from the CC0.5 run product exhibit an elongate bladed habit (Fig. 4b). No change in morphology was observed with increasing time and decreasing temperature, although crystals become more elongated and branched. We observed a morphological difference in the iron oxides that exhibit an equant shape under single-step cooling (in SSC1150) and a skeletal form under continuous cooling (in CC0.5).

244

4. Discussion

4.1. Single-step versus continuous cooling: differences in mineralogical assemblages and kinetics

4.1.1. Mineralogical differences

Depending on the type of cooling (single-step vs continuous), we noticed the presence or absence of clinopyroxene and plagioclase. Clinopyroxene is present in both single-step experiments, although in a very small amount in SSC1170, from near the beginning of the dwell period (after 12 min dwell in SSC1150, Polacci et al., 2018), while plagioclase remains absent until the final cooling stage (Arzilli et al., 2019), occurring as skeletal crystals. On the contrary, only plagioclase crystallised from the melt on continuous cooling (CC0.5), with the occurrence of minor clinopyroxenes (too small for analysis by EPMA) during the final

256   cooling to room temperature. For comparison, the equilibrium assemblage calculated by

257   MELTS software (Ghiorso and Sack, 1995; Asimow and Ghiorso, 1998), at ambient pressure

258   and fugacity (magnetite-hematite MH redox buffer), comprises both plagioclase ($T_{liquidus}$ =

259   1208 °C) and clinopyroxene ($T_{liquidus}$ = 1188 °C). As discussed above (section 3.1), the

260   texture of the SS1170 charge suggests that the liquidus temperature of clinopyroxene is closer

261   to 1170 °C. This enabled us to determine the nucleation undercooling ($\Delta T = T_{liquidus} -$

262    $T_{experimental}$) as a function of temperature: for clinopyroxene $\Delta T = 0$ °C at 1170 °C and 20 °C

263   at 1150 °C, for plagioclase $\Delta T = 0$ °C at 1220 °C, 38 °C at 1170 °C and 58 °C at 1150 °C.

264   Both the SSC1170 and SSC1150 experiments were thus run below the predicted plagioclase

265   liquidus, meaning that plagioclase should have been present within the 4-h dwell. Similarly,

266   we performed part (80 min) of the CC0.5 experiment below the clinopyroxene liquidus

267   without nucleating clinopyroxene crystals. In each cooling regime, the nucleation of one

268   crystal phase is suppressed, attesting to disequilibrium crystallisation.

269   The absence of either plagioclase or clinopyroxene in cooling-induced crystallisation

270   experiments, while it should be thermodynamically stable, was reported previously by some

271   authors (e.g. Corrigan, 1982; Gibb, 1974; Lofgren, 1983; Vetere et al., 2015). They mainly

272   attribute the failure of these phases to nucleate to the degree of undercooling (a large ΔT, or

273   high cooling rate, inhibiting the nucleation of plagioclase), a limited experimental duration

274   and a low number of heterogeneous nucleation sites. In our SSC1150 single-step experiment,

275   the nucleation of clinopyroxene followed a rapid (24 °C/min) temperature drop that drove a

276   rapid increase of undercooling to 20 °C for clinopyroxene and to 58 °C for plagioclase, and

277   brought the melt to sub-liquidus conditions where both phases can grow. However, although

278   the nucleation of clinopyroxene was activated after 12 min at constant temperature,

279   plagioclase was not able to crystallise within the 4 h dwell. This indicates first that time plays

12

280   a major role in the evolution of crystallisation, and second that clinopyroxene needs lower

281   activation energy to nucleate, associated with its lower number of tetrahedral units (Al–O and

282   Si–O bonds) and less polymerised structure in comparison to plagioclase, which in turn

283   translates into a shorter delay in nucleation (Iezzi et al., 2008). In addition, following these

284   relatively fast nucleation and growth, the residual melt became depleted in clinopyroxene

285   components (Ca, Mg, Fe, Table A.1), possibly delaying the stabilization of plagioclase

286   nuclei. In contrast, and despite its more complex structure, the slow cooling rate of 0.5

287   °C/min enabled the nucleation of plagioclase. This suggests that suppression of crystal

288   nucleation is not simply related to structural control alone, as previously suggested by

289   Corrigan (1982). Following the nucleation and growth of plagioclase crystals near the

290   liquidus temperature, the residual melt became depleted in plagioclase components

291   (anorthite: Ca and Na, Table A.1), creating a local disequilibrium that may have delayed the

292   formation of clinopyroxene. Nucleation sites for clinopyroxene may also be missing. They

293   may have been suppressed because of a longer time spent above their liquidus temperature

294   (122 min for CC0.5 instead of 3 min for SSC1150, from the end of melting/homogenisation)

295   or occupied by early-formed plagioclase crystals.

296   Our observations show that the cooling rate and the resulting increase of undercooling

297   through time are important factors controlling crystallisation. In this sense, Vetere et al.

298   (2015) documented that plagioclase is only able to crystallise at low to moderate cooling

299   rates (< 3 °C/min). However, Arzilli et al. (2019) observed the crystallisation of plagioclase

300   at a high cooling rate of 24 °C/min. The difference may be related to initial conditions, since

301   superheating, as applied by Vetere et al. (2015), can promote an efficient dissolution of pre-

302   existing nuclei (e.g. Arzilli et al., 2015), while a time-step at sub-liquidus conditions can

303   promote the formation of stable nuclei, which once subjected to a rapid thermal perturbation

304   of the system are able to grow rapidly. The effects of thermal history on the mineralogical

13

305   assemblage of cooling basalts appear to be not yet well understood, stressing that more

306   systematic real-time investigations should be performed.

307

308   *4.1.2. Crystal nucleation kinetics*

309   The experimental charges have higher crystal abundances at the gas-melt and container-melt

310   interfaces because of the lower surface free energy required for nucleation. At the container

311   walls, the heterogeneous nucleation of plagioclase and clinopyroxene crystals is associated

312   with the presence of tiny air bubbles and the early formation of Al–Mg oxides (Fig. A.4),

313   both acting as nucleation sites. The presence of pre-existing nuclei is an important

314   mechanism that contributes to the solidification of basaltic lava flows (e.g. Mollo et al.,

315   2015), emphasising that *in situ* observations can unravel the dynamics of heterogeneous

316   crystal nucleation and its important implications on the development of basaltic textures, and

317   so on conduit processes and eruptive dynamics.

318   In addition to being reduced by heterogeneous nucleation, the nucleation delay, i.e. the time

319   between when the melt is brought below its liquidus and the onset of nucleation (Rusiecka et

320   al., 2020), is reduced as a function of undercooling. As expected with increasing

321   undercooling and/or experimental duration (e.g. Rusiecka et al., 2020 and references therein;

322   Vona and Romano, 2013), the nucleation of clinopyroxene occurs faster and the volume

323   fraction of crystals increases (Fig. 3). The plagioclase-free texture of the SSC1150 sample,

324   during the 4-h dwell, is also consistent with the findings of Rusiecka et al. (2020).

325   In contrast to previous *in situ* research (Ni et al., 2014) that reports the nucleation of olivine

326   or clinopyroxene crystals only in a short event of a few minutes at the beginning of the

327   experiment, we observed multiple nucleation events up to t_2 (160 min dwell/cooling) and the

328   continuous growth of both clinopyroxene (SSC1150) and plagioclase crystals (CC0.5). These

329   multiple nucleation events, reported as two main nucleation/growth pulses in SSC1150 (at 60

330   and 150 min dwell) in Polacci et al. (2018), may be induced by changes in melt composition

331   with further effects on the liquidus temperature, following the nucleation and growth of first

332   crystals. Such multiple nucleation events have been recently reported by Giuliani et al. (2020)

333   to account for the formation of clinopyroxene in basaltic melt.

334

335   *4.1.3. Crystal growth kinetics*

336   In the time interval of our experiments, clinopyroxene and plagioclase crystals grew at rates

337   of 10^{-6} cm/s and 10^{-5}–10^{-6} cm/s, respectively. A clinopyroxene growth rate of 10^{-6} cm/s is

338   similar to, or higher than, the one reported in previous works on anhydrous basaltic and

339   trachybasaltic melts (10^{-6}–10^{-9} cm/s, Baker, 2008; Burkhard, 2005; Giuliani et al., 2020; Ni et

340   al., 2014; Orlando et al., 2008; Pontesilli et al., 2019). Lower growth rates of 10^{-7}–10^{-9} cm/s

341   have been reported for plagioclase crystals (Arzilli et al., 2015; Giuliani et al., 2020; Orlando

342   et al., 2008). These differences are associated with the use of *in situ* data, since we measured

343   dynamic growth rates that are known to decrease with increasing dwell time (e.g. Pontesilli et

344   al., 2019), with impingement by surrounding crystals. *Ex situ*, growth rates are determined

345   for entire experimental periods and are thus averaged and possibly underestimated. In

346   addition, the use of 2D data provides less accurate shape information.

347   At constant undercooling ($\Delta T = 20$ °C), the clinopyroxene growth rate by size (Y_{L3D}) is

348   nearly constant through time, and the volumetric growth rate (Y_v) slightly increases (Fig. 5).

349   With increasing undercooling by 20 °C, from 38 °C to 58 °C, both the Y_{L3D} and Y_v

350   plagioclase growth rates quadruple (Fig. 5). Kirkpatrick (1975) also showed an increase of

351   the rate of crystal growth with increasing undercooling for a large temperature range.

15

352   Following Tamman (1899) and as predicted by the theory (Kirkpatrick, 1975), we can expect

353   the rate of crystal growth to be near-zero at the liquidus, increase to a maximum and then

354   decrease with increasing undercooling.

355   The initially individual clinopyroxene and plagioclase crystals grew along

356   thermodynamically favourable directions, i.e. perpendicular to the surface of heterogeneities

357   (Al-walls of the sample holder, air bubbles and first-nucleated crystals, including many

358   oxides), forming networks of agglomerated crystals (Fig. 3). Clinopyroxene crystals grew

359   radially from the top of the VoI and the edge walls of the alumina container, mainly by

360   branching and aggregation (Fig. 3d–f). Plagioclases also align along preferential directions,

361   perpendicular to the sample holder (Fig. 3g–i). The euhedral textures developed by both the

362   clinopyroxenes and titanomagnetites in SSC1150 result from interface-controlled growth

363   mechanisms, which are favoured by a small undercooling of 20 °C and a high temperature of

364   1150 °C that is close to the liquidus temperature of 1170 °C. In contrast, the plagioclase

365   blades observed in CC0.5 indicate some disequilibrium between the melt and crystals, linked

366   to larger undercoolings and departure from their liquidus temperature (1208 °C). The shape

367   of these rapidly growing crystals is controlled by diffusion, with a slow diffusivity of cations

368   in the melt (Mollo and Hammer, 2017). Attainment of equilibrium did not occur during the

369   course of the continuous cooling experiment (~5 h) for plagioclase. In that experiment, the

370   oxide crystals are skeletal, which also attests to their development under conditions of rapid

371   growth and high degrees of undercooling.

372   Aggregation of smaller and mutually touching crystals was reported to occur in Etnean

373   pāhoehoe and ʻaʻā lavas at syn-eruptive conditions over the effect of undercooling (e.g.

374   Lanzafame et al., 2013). This underlines the close reproducibility of the near-surface

375   crystallisation of basaltic melts by our innovative *in situ* approach and thus its utility in lava

376   flow studies.

16

377

4.1.3. Rheology of the crystal-bearing samples

Growing crystals increase the viscosity of the suspending basaltic lava and introduce non-Newtonian rheology (e.g. Giordano et al., 2008; Mueller et al., 2010; Vona et al., 2011), which in turn affects its transport (e.g. Soldati et al., 2016). Assessing the rheological evolution of crystallising basaltic melts is thus required for lava flow modelling, to predict how the lava flow will evolve in time and space. Here, we infer the evolving rheology of our SSC1150 and CC0.5 crystal-bearing samples from a Hershel-Bulkley model (Herschel and Bulkley, 1926; Mader et al., 2013):

$$\tau = \tau_0 + K\dot{\gamma}^n \,, \qquad\qquad \text{Eq. 1}$$

where τ is the shear stress, τ_0 is a yield stress, K is the consistency, $\dot{\gamma}$ is the strain-rate and n is the flow index. The rheological impact of the crystal phase depends primarily on the ratio of the crystal volume fraction ϕ to the maximum crystal packing fraction ϕ_m (ϕ/ϕ_m) because τ_0, K and n are all functions of ϕ/ϕ_m (Mader et al., 2013). ϕ_m can be calculated from the aspect ratio of the crystals r_p (Mader et al., 2013; Mueller et al., 2010):

$$\phi_m = 0.55 \exp\left[-\frac{\left(\log_{10} r_p\right)^2}{2}\right]. \qquad\qquad \text{Eq. 2}$$

Both ϕ and r_p are measured directly from our *in situ* data (Section 2.3.1). SSC1150 contains clinopyroxene crystals with average aspect ratios of 4.07 (60 min dwell), 7.41 (160 min dwell) and 7.35 (200 min dwell, Tables 2 and A.2), and CC0.5 contains plagioclase crystals with average r_p of 4.24 (160 min cooling) and 5.76 (200 min cooling, Tables 2 and A.3). Consistency and flow index are calculated following Mader et al. (2013):

$$K = \mu_0 \left(1 - \frac{\phi}{\phi_m}\right)^{-2}, \qquad\qquad \text{Eq. 3}$$

$$n = 1 - 0.2 r_p \left(\frac{\phi}{\phi_m}\right)^4, \qquad\qquad \text{Eq. 4}$$

396 where μ_0 is the viscosity of the melt phase, which can be calculated as a function of

397 composition and temperature (Giordano et al., 2008). At 1170 °C and 1150 °C, the viscosities

398 of melt samples are respectively of 2.01 and 2.18 log Pa s. Computed values of ϕ_m, the ratio

399 ϕ/ϕ_m, K and n are tabulated in Table 2.

400 Mader et al. (2013) show that τ_0 is negligible for $\phi/\phi_m < 0.8$, which is the case for all of our

401 tomographic reconstructions. In this case, Equation 1 reduces to a power law in which

402 suspension viscosity η depends on strain rate:

$$\eta = K \dot{\gamma}^{n-1}. \qquad\qquad \text{Eq. 5}$$

403 They further argue that shear thinning effects can be neglected for most strain rates of

404 practical interest if $n \geq 0.9$, which is the case for most of our tomographic reconstructions. In

405 this case, $\eta \equiv K$ and the Newtonian suspension viscosity can be calculated directly using

406 Equation 3.

407 Results (Tables 2, A2 and A3) show that our samples exhibit a Newtonian behaviour during

408 both the dwell and continuous cooling, with small ϕ/ϕ_m of 0.02 at t_1 to 0.24 at t_3 in SSC1150

409 and of 0.20 at t_1 to 0.53 at t_3 in CC0.5, respectively. However, higher values of this ratio

410 (0.64 in SSC1150 and 0.58 in CC0.5) are expected after more than the 200 min

411 dwell/cooling, by considering a maximum ϕ of 0.24 as found in the LV magmas (Corsaro et

412 al., 2007). With more time, our two samples produced under different temperature-time

413 conditions, would thus evolve towards a non-Newtonian behaviour, with consequences for

414 magma transport (see Section 4.2).

415 Magma viscosity is also dependent on shear rate, which facilitates the nucleation and growth

416 of crystals (Vona and Romano, 2013). During transport and emplacement, magmas and lavas

417 undergo a range of shear rates (2.5–0.001 s^{-1}, Kolzenburg et al., 2018 and references therein).

418 Although we did not investigate the effect of varying the deformation rate on the rheological

419 evolution of crystallising basaltic melts, previous experimental studies (Kolzenburg et al.,

420 2018; Tripoli et al., 2019; Vona et al., 2011; Vona and Romano, 2013) showed that shear

421 deformation accelerates crystallisation kinetics, resulting in shorter nucleation delays and

422 higher crystal fractions.

423 In more detail, Vona et al. (2011) performed *ex situ* isothermal crystallisation experiments

424 while capturing the temporal evolution of the viscosity of anhydrous Etna basalt of the 1991–

425 1993 eruption deformed under a low strain rate of 0.53 s^{-1}. In air, at 1157 °C and 1 atm,

426 crystallisation takes place within 29–45 h, associated with an increase in apparent viscosity to

427 a stable value of 3.07 log Pa s ($\phi = 0.16$). The final mineralogical assemblage is composed of

428 spinel (minor) and plagioclase, which differs from our SSC1150 experiment, where

429 clinopyroxene nucleated after a short 12-min delay. Their starting melt composition slightly

430 differs from ours, but not enough to justify such a difference in crystallisation time, as well as

431 in the order of nucleation of crystal phases. We suggest, instead, that these differences can be

432 explained by a longer time spent above the liquidus temperature (5h at 1400 °C in Vona et

433 al., 2011 vs 30 min at 1250 °C in our study), which allows a more complete dissolution of

434 pre-existing nuclei. These differences can also be explained by the use of a different

435 apparatus (concentric cylinder viscometer) equipped with a spindle that causes chemical

436 heterogeneities and mechanical perturbations in the melt (Vona et al., 2011). Recent findings

437 (e.g. Tripoli et al., 2019; Kolzenburg et al., 2020) demonstrated that in the absence of thermal

438 and/or mechanical fluctuations the nucleation of plagioclase is not favoured, as observed in

439 our single-step experiments.

440   Using the model of Vona et al. (2011), which considers the magma strain rate and both the

441   crystal fraction and crystal shape factors (Vona and Romano, 2013), we calculated the

442   relative viscosity of our SSC1150 suspensions (liquid + crystal, considering both

443   clinopyroxene and oxide phases). As expected (Vona et al., 2011 and references therein), the

444   relative viscosity increases with increasing crystal fraction ϕ, from 1.21 log Pa s at $\phi = 0.05$

445   (t_1, Table 2) to 2.39 log Pa s at $\phi = 0.14$ (t_2, Table 2) to 3.37 log Pa s at $\phi = 0.17$ (t_3, Table 2).

446   According to Polacci et al. (2018), a stable clinopyroxene crystal content (~14 vol%) can be

447   reached after ~500–1500 min dwell (~8–25 h) in the SSC1150 sample, which translates to a

448   higher relative viscosity of 6.93 log Pa s at $\phi = 0.22$ (including a stable oxide content of 8

449   vol%, Arzilli et al., 2019).

450   Kolzenburg et al. (2018) were among the first to study the effect of shear rate at non-

451   isothermal conditions, which can be related to our CC0.5 continuous cooling experiment.

452   They observed that the onset temperature of crystallisation increases with increasing shear

453   rate, from 1101 °C (no shear) to 1164 °C and 1178 °C for shear rates of 1.16 and 4.64 s^{-1},

454   respectively, at a cooling rate of 0.5 °C/min and using a trachybasalt from the 2013 eruption

455   of Etna. However, in CC0.5 crystallisation occurs at high temperatures (~1205 °C) without

456   introducing shear, suggesting that results can hardly be compared with each other. Here

457   again, differences can be due to the use of a concentric cylinder apparatus with a longer time

458   spent above the liquidus temperature (several hours at 1300 °C) and more reduced conditions,

459   and a slightly different starting melt composition. Kolzenburg et al. (2018) also showed that

460   increasing shear rate increases the cutoff temperature (T_{cutoff}, i.e. the point at which the

461   sample rheologically solidifies and flow stops), which implies shorter flow distances.

462   Although it is not relevant to our data, if deformation is taken into account, transitions

463   between different eruptive styles or flow mechanisms can occur in a shorter amount of time

464   (Vona and Romano, 2013).

465

466 *4.2. Implications for basaltic lava flows*

467 *4.2.1. Time evolution of magma crystallinity: the pāhoehoe-ʻaʻā transition*

468 As described above, our results can be used to investigate the effect of cooling and

469 crystallisation on the rheological properties of lava, and more specifically to retrieve the

470 conditions under which pāhoehoe lavas transform to ʻaʻā. Such a transition is greatly

471 influenced by the viscosity of the lava, which is dependent on temperature and crystallinity,

472 and associated with the development of yield strength (Cashman et al., 1999). A critical

473 crystallinity range at which pāhoehoe transforms to ʻaʻā has been identified between 0.18 and

474 0.35 (Hon et al., 2003; Soule et al., 2004), although some Etnean pāhoehoe lavas (termed

475 "cicirara") can contain up to 40 vol% crystals (e.g. Lanzafame et al., 2013). We inferred such

476 parallel changes of crystallinity and rheological behaviour (onset of non-Newtonian

477 behaviour) after more than 200 min dwell/cooling at a comparable crystallinity of 0.24, as

478 found in the 2001 trachybasalts. In addition, a critical viscosity range for the pāhoehoe–ʻaʻā

479 transition has been calibrated from a combination of field observations and laboratory

480 experiments, from 4 log Pa s (no shear rate) to ~2.7 log Pa s with increasing shear rate (e.g.

481 Cashman and Mangan, 2014, and references therein; Sehlke et al., 2014; Soldati et al., 2017).

482 In line with this finding, such viscosities are approached in our single-step cooling conditions

483 (SSC1150) after 200 min and largely exceeded within 8 h. Under our given *P-T-f*O_2-

484 composition conditions, the transition of basaltic lava from pāhoehoe to ʻaʻā can thus be

485 crossed in ca. 4 h from emission under continuous cooling, or between 3 and 8 h under

486 single-step cooling.

487

4.2.2. Crystallisation timescales in basaltic lava flows and the case study of the 2001

489 *eruption of Mt. Etna*

490 Under single-step cooling (near-isothermal) conditions, our data coupled with the empirical

491 model of Polacci et al. (2018) indicate that 14 vol% of crystals (single-phase) can nucleate

492 and grow over a day. This amount alone is not enough to bring a major shift in rheological

493 behaviour, implying that lava can travel great distances with minimal cooling. Under

494 continuous cooling (non-isothermal) conditions, our results demonstrate that the growth of 22

495 vol% plagioclase crystals in just over 3 h would soon have a significant impact on flow

496 behaviour. According to Kolzenburg et al. (2020), the lava could solidify and stop flowing

497 after reaching 1128 °C, i.e. after 244 min (~4 h) of continuous cooling at 0.5 °C/min. During

498 flowage onto the surface, the behaviour of basaltic lavas appears to be greatly influenced by

499 both temperature and time, with crystal phases possibly nucleating and growing under

500 different cooling regimes, as explored below.

501 As a trachybasalt from the 2001 Etna eruption was used as the starting material for our

502 experimental simulations of lava flow emplacement, results can aid in the interpretation of

503 the final crystallisation history of the erupted LV lavas. According to Lanzafame et al. (2013)

504 who unravelled the solidification path of a pāhoehoe lava from Mt. Etna through petrographic

505 analysis, crystals with a size <1 mm (~75 vol%) crystallised during lava emplacement. Our

506 results agree well with this finding, since the SSC1150 single-step cooled sample crystallised

507 the amount of clinopyroxene phenocrysts found in the 2001 lavas (~9–14 vol%) within 200

508 to 500–1500 min of dwell (Polacci et al., 2018) at 1150 °C. After that time, a critical

509 crystallinity (of maximum 24 vol%) could be reached with the appearance of a second

510 phenocryst phase (6–7 vol% plagioclase) in the same proportions as in the 2001 LV products.

511 For comparison, in the CC0.5 sample, continuously cooled at a rate of 0.5 °C/min, 4 to 7

512 vol% plagioclase crystals appeared in less than 160 min at $T \geq 1170$ °C. However, 40 min

513   later (T = 1150 °C) CC0.5 already contained 22 vol% plagioclase and no clinopyroxene,

514   which differs strongly from the LV products. In addition to reproduce the abundance of

515   clinopyroxene crystals in the SSC1150 experiment, we reproduced their composition with an

516   average Mg number (Mg#) of 72 vs of 73 in the LV products (Fig. 6). According to Mollo et

517   al. (2015), the Mg#$_{54–74}$ clinopyroxene population in Etna products formed within the range

518   of our experimental conditions, i.e. at 0.1–500 MPa and 1050–1175 °C. LV textures are thus

519   very well reproduced by our single-step experiment at 1150 °C, meaning first that the interior

520   of lava flows in the 2001 eruption may have cooled almost isothermally, and second that the

521   nucleation of clinopyroxene may have occurred in the shallowest portion of the Etnean

522   plumbing system and during lava transport at the surface. However, this excludes the few

523   larger (3–10 mm) clinopyroxene crystals present in the LV lavas, which cannot be

524   reproduced by our experiments, and that result from crystallisation at depth during storage

525   (Mollo et al., 2015 and references therein), as well as olivine crystals that nucleated and grew

526   under water-saturated conditions at high pressures and temperatures (Mollo et al., 2015). The

527   nucleation of plagioclase seems to have happened differently. According to La Spina et al.

528   (2016), the low plagioclase content in the 2001 LV products indicates a fast (<1 h) vertical

529   ascent from depth (9 km) to the surface. Plagioclase crystals might have nucleated and grew

530   during ascent under non-equilibrium conditions, and not during flow advance, driven by

531   magma degassing (Mollo et al., 2015). In accordance with it, both the lower range of

532   plagioclase core compositions and rim compositions (An$_{64}$, Corsaro et al., 2007) were

533   reproduced in the SSC1150 experiment (An$_{67}$, Fig. 6 and Table A.1), implying that

534   plagioclases in the LV trachybasalts did not nucleate outside of the conduit, although their

535   growth was affected by subaerial conditions. The interior of the 2001 lava flows could thus

536   result from a combination of pre-, syn- and post-eruptive crystallisation.

23

As demonstrated with our study, working *in situ* enables the solidification of a basaltic lava flow to be directly observed, and so reproduced with varying both time and temperature. This opens new perspectives to unravel the solidification path of basaltic lavas, especially as only a small amount of phenocrysts could equilibrate at depth, with most of the crystallisation happening during magma ascent in the conduit and emplacement to the surface (Lanzafame et al., 2013; Giuliani et al., 2020), which are conditions that we can simulate with our *in situ* equipment.

5. Conclusions

Our results from single-step *versus* continuous cooling experiments show that cooling rate and undercooling have a strong influence on the nucleation of clinopyroxene and plagioclase, with implications for the behaviour of basaltic lavas. According to our 3D time-dependent observations combined with published rheological data, the interior of the 2001 lava flows of Etna may have crystallised up to 14 vol% clinopyroxene phenocrysts almost isothermally over a day. Such a nucleation and growth of crystals during lava flow emplacement accompanies changes in rheological behaviour, which affect lava flow length and hazard severity.

568

569   References

570   Abramoff, M. D., Magalhaes, P. J., Ram, S. J., 2004. Image processing with ImageJ.

571   Biophotonics Int. 11, 36–42.

572   Arzilli, F., Mancini, L., Voltolini, M., Cicconi, M.R., Mohammadi, S., Giuli, G., Mainprice,

573   D., Paris, E., Barou, F., Carroll, M.R., 2015. Near-liquidus growth of feldspar

574   spherulites in trachytic melts: 3D morphologies and implications in crystallization

575   mechanisms. Lithos. 216–217, 93–105. https://doi.org/10.1016/j.lithos.2014.12.003

576   Arzilli, F., La Spina, G., Burton, M.R., Polacci, M., Le Gall, N., Hartley, M.E., Di Genova,

577   D., Cai,B., Vo, N.T., Bamber, E.C., Nonni, S., Atwood, R., Llewellin, E.W., Brooker,

578   R.A., Mader,H.M., Lee, P.D., 2019. Magma fragmentation in highly explosive

579   basaltic eruptions induced by rapid crystallization. Nat. Geosci. 12, 1023–1028.

580   https://doi.org/10.1038/s41561-019-0468-6

581   Asimow, P. D., Ghiorso, M. S., 1998. Algorithmic modifications extending MELTS to

582   calculate subsolidus phase relations. Am. Mineral. 83, 1127–1132.

583   https://doi.org/10.2138/am-1998-9-1022

584   Azeem, M. A., Lee, P.D., Phillion, A.B., Karagadde, S., Rockett, P., Atwood, R.C., Courtois,

585   L., Rahman, K.M., Dye, D., 2017. Revealing dendritic pattern formation in Ni, Fe and

586   Co alloys using synchrotron tomography. Acta Mater. 128, 241–248.

587   https://doi.org/10.1016/j.actamat.2017.02.022

588   Baker, D.R., 2008. The fidelity of melt inclusions as records of melt composition. Contrib.

589   Mineral. Petrol. 156, 377–395. https://doi.org/10.1007/s00410-008-0291-3

590   Baker, D.R., Mancini, L., Polacci, M., Higgins, M.D., Gualda, G.A.R., Hill, R.J., Rivers,

591   M.L., 2012. An introduction to the application of X-ray microtomography to the

592   three-dimensional study of igneous rocks. Lithos 148, 262–276.

593   https://doi.org/10.1016/j.lithos.2012.06.008

594   Burkhard, D.J.M., 2005. Nucleation and growth rates of pyroxene, plagioclase, and Fe–Ti

595   oxides in basalt under atmospheric conditions. Eur. J. Mineral. 17, 675–685.

596   https://doi.org/10.1127/0935-1221/2005/0017-0675

597   Cashman, K.V., Mangan, M.T., 2014. A century of studying effusive eruptions in Hawai'i.

598   Characteristics of Hawaiian volcanoes. U.S.G.S. Prof. Paper 1801-9:357–394.

599   http://dx.doi.org/10.3133/pp18019

600   Cashman, K.V., Thornber, C., Kauahikaua, J.P., 1999. Cooling and crystallization of lava in

601   open channels, and the transition of pahoehoe to aa. Bull. Volcanol. 61, 306–323.

602   https://doi.org/10.1007/s004450050299

603   Corrigan, G., 1982. Supercooling and the crystallization of plagioclase, olivine, and

604   clinopyroxene from basaltic magmas. Mineral Mag. 46, 31–42.

605   Corsaro, R.A., Miraglia, L., Pompilio, M., 2007. Petrologic evidence of a complex plumbing

606   system feeding the July–August 2001 eruption of Mt. Etna, Sicily, Italy. Bull.

607   Volcanol. 69, 401–421. https://doi.org/10.1007/s00445-006-0083-4

608   Drakopoulos, M., Connolley, T., Reinhard, C., Atwood, R., Magdysyuk, O., Vo, N., Hart,

609   M., Conner, L., Humphreys, B., Howell, G., Davies, S., Hill, T., Wilkin, G., Pedersen,

610   U., Foster, A., De Maio, N., Basham, M., Yuan, F., Wanelik, K., 2015. J. Synchrotron

611   Rad. 22, 828–838. https://doi.org/10.1107/S1600577515003513

612   Ghiorso, M. S., Sack, R. O., 1995. Chemical mass transfer in magmatic processes IV. A

613   revised and internally consistent thermodynamic model for the interpolation and

614   extrapolation of liquid-solid equilibria in magmatic systems at elevated temperatures

615   and   pressures.   Contrib.   Mineral.   Petrol.   119,   197–212.

616   https://doi.org/10.1007/BF00307281

617   Gibb, F.G.F., 1974. Supercooling and the crystallization of plagioclase from a basaltic

618   magma. Min. Mag. 39, 641–653. https://doi.org/10.1180/minmag.1974.039.306.02

619   Giordano, D., Russell, J.K., Dingwell, D.B., 2008. Viscosity of magmatic liquids: a model.

620   Earth Planet Sci. Lett. 271, 123–134. http://dx.doi.org/10.1016/ j.epsl.2008.03.038.

621   Giuliani, L., Iezzi, G., Vetere, F., Behrens, H., Mollo, S., Cauti, F., Ventura, G., Scarlato, P.,

622   2020. Evolution of textures, crystal size distributions and growth rates of plagioclase,

623   clinopyroxene and spinel crystallized at variable cooling rates from a mid-ocean ridge

624   basaltic   melt.   Earth   Sci.   Rev.   204:103165.

625   https://doi.org/10.1016/j.earscirev.2020.103165

626   Gürsoy, D., De Carlo, F., Xiao, X., Jacobsen, C., 2014. Tomopy: a framework for the

627   analysis of synchrotron tomographic data. J. Synchrotron Rad. 21, 1188–1193.

628   https://doi.org/10.1107/S1600577514013939

629   Herschel, W.H., Bulkley, R., 1926. Konsistenzmessungen von gummi-benzollösungen.

630   Kolloid-Zeitschrift, 39, 291–300. https://doi.org/10.1007/BF01432034

631   Hon, K.A., Gansecki, C., Kauahikaua, J., 2003. The transition from 'a'ā to pāhoehoe crust on

632   flows emplaced during the Pu'u 'Ō'ō-Kūpaianaha eruption. USGS Prof. Pap. 1676

633   89–103.

634   Iezzi, G., Mollo, S., Ventura, G., Cavallo, A., Romano, C., 2008. Experimental solidification

635   of anhydrous latitic and trachytic melts at different cooling rates: the role of

636   nucleation kinetics. Chem. Geol. 253, 91–101.

637   Kirkpatrick, R.J., 1975. Crystal growth from the melt: A review. Am. Mineral. 60, 798–814.

638   Kolzenburg, S., Giordano, D., Hess, K.U., Dingwell, D.B., 2018. Shear rate-dependent

639   disequilibrium rheology and dynamics of basalt solidification. Geophys. Res. Lett. 45,

640   6466–6475. https://doi.org/10.1029/2018GL077799

641   Kolzenburg, S., Hess, K.U., Berlo, K., Dingwell, D.B., 2020. Disequilibrium rheology and

642   crystallization kinetics of basalts and implications for the Phlegrean volcanic District.

643   Front. Earth Sci. 8:187. doi: 10.3389/feart.2020.00187

644   La Spina, G., Burton, M. R., de'Michieli Vitturi, M., Arzilli, F., 2016. Role of syn-eruptive

645   plagioclase disequilibrium crystallization in basaltic magma ascent dynamics. Nat.

646   Commun. 7, 13402. https://doi.org/10.1038/ncomms13402

647 Lanzafame, G., Mollo, S., Iezzi, G., Ferlito, C., Ventura, G., 2013. Unraveling the
648   solidification path of a pahoehoe "cicirara" lava from Mount Etna volcano. Bull.
649   Volcanol. 75, 703. https://doi.org/10.1007/s00445-013-0703-8

650 Lofgren, G.E., 1983. Effect of heterogeneous nucleation on basaltic textures: a dynamic
651   crystallization study, J. Petrol. 24, 229–255.
652   https://doi.org/10.1093/petrology/24.3.229

653 Mader, H.M., Llewellin, E.W., Mueller, S.P., 2013. The rheology of two-phase magmas: a
654   review and analysis. J. Volcanol. Geotherm. Res. 257, 135–158.
655   https://doi.org/10.1016/j.jvolgeores.2013.02.014

656 Mollo, S., Hammer, J.E., 2017. Dynamic crystallization in magmas. EMU Notes Mineral. 16,
657   373–418. https://doi.org /10.1180/EMU-notes.16.12.

658 Mollo, S., Giacomoni, P.P., Coltorti, M., Ferlito, C., Iezzi, G., Scarlato, P., 2015.
659   Reconstruction of magmatic variables governing recent Etnean eruptions: constraints
660   from mineral chemistry and P–T–fO$_2$–H$_2$O conditions. Lithos 212–215, 311–320.

661 Mueller, S., Llewellin, E.W., Mader, H.M., 2010. The rheology of suspensions of solid
662   particles. Proceedings of the Royal Society A: Mathematical, Physical and
663   Engineering Sciences, 466(2116), 1201–1228. https://doi.org/10.1098/rspa.2009.0445

664 Ni, H., Keppler, H., Walte, N., Schiavi, F., Chen, Y., Masotta, M., Li, Z., 2014. In situ
665   observation of crystal growth in a basalt melt and the development of crystal size
666   distribution in igneous rocks. Contrib. Mineral. Petrol. 167, 1–13. https://
667   doi.org/10.1007/s00410- 014- 1003- 9.

668 Orlando, A., D'Orazio, M., Armienti, P., Borrini, D., 2008. Experimental determination of
669   plagioclase and clinopyroxene crystal growth rates in an anhydrous trachybasalt from

670   Mt Etna (Italy). Eur. J. Mineral. 20, 653–664. https://doi.org/ 10.1127/0935-

671   1221/2008/0020- 1841.

672 Peterson, D.W., Tilling, R.I., 1980. Transition of basaltic lava from pahoehoe to aa, Kilauea

673   Volcano, Hawaii: field observations and key factors. J. Volcanol. Geotherm. Res. 7,

674   271–293. https://doi.org/10.1016/0377-0273(80)90033-5

675 Polacci, M., Arzilli, F., La Spina, G., Le Gall, N., Cai, B., Hartley, M.E., Di Genova, D., Vo,

676   N.T., Nonni, S., Atwood, R.C., Llewellin, E.W., Lee, P.D., Burton, M.R., 2018.

677   Crystallisation in basaltic magmas revealed via in situ 4D synchrotron X-ray

678   microtomography. Sci. Rep. 8, 8377–8383. https://doi.org/10.1038/s41598-018-

679   26644-6.

680 Pontesilli, A., Masotta, M., Nazzari, M., Mollo, S., Armienti, P., Scarlato, P., Brenna, M.,

681   2019. Crystallization kinetics of clinopyroxene and titanomagnetite growing from a

682   trachybasaltic melt: new insights from isothermal time-series experiments. Chem.

683   Geol. 510, 113–129. https://doi.org/10.1016/j.chemgeo.2019.02.015

684 Rusiecka, M. K., Bilodeau, M., Baker, D. R., 2020. Quantification of nucleation delay in

685   magmatic systems: experimental and theoretical approach. Contribut. Mineral. Petrol.

686   175:47. https://doi.org/10.1007/s00410-020-01682-4

687 Schiavi, F., Walte, N., Keppler, H., 2009. First in situ observation of crystallization processes

688   in a basaltic–andesitic melt with the moissanite cell. Geology. 37, 963–966.

689   https://doi.org/10.1130/G30087A.1

690 Sehlke A., Whittington, A., Robert, B., Harris, A., Gurioli, L., Médard, E., 2014. Pahoehoe to

691   `a`a transition of Hawaiian lavas: an experimental study. Bull. Volcanol. 76, 876.

692   https://doi.org/10.1007/s00445-014-0876-9

693   Soldati, A., Sehlke, A., Chigna, G., Whittington, A., 2016. Field and experimental constraints

694   on the rheology of arc basaltic lavas: the January 2014 Eruption of Pacaya

695   (Guatemala). Bull. Volcanol. 78, 43. https://doi.org/10.1007/s00445-016-1031-6

696   Soldati, A., Beem, J., Gomez, F., Huntley, J.W., Robertson, T., Whittington, A., 2017.

697   Emplacement dynamics and timescale of a Holocene flow from the Cima Volcanic

698   Field (CA): Insights from rheology and morphology. J. Volcanol. Geotherm. Res.

699   347, 91–111. https://doi.org/10.1016/j.jvolgeores.2017.09.005

700   Soule, S.A., Cashman, K.V., Kauahikaua, J.P., 2004. Examining flow emplacement through

701   the surface morphology of three rapidly emplaced, solidified lava flows, Kilauea

702   Volcano, Hawaii. Bull. Volcanol. 66, 1–14.

703   Tamman, G., 1899. Über die abhangigkeidt der zahl der kerne. Z. Phys. Chem. 25, 441–479.

704   Titarenko, V., Titarenko, S., Withers, P.J., De Carlo, F., Xiao, X., 2010. Improved

705   tomographic reconstructions using adaptive time-dependent intensity normalization. J.

706   Synchrotron Radiat. 17, 689–699. https://doi.org/10.1107/S0909049510024908

707   Tripoli, B., Manga, M., Mayeux, J., Barnard, H., 2019. The effects of deformation on the

708   early crystallization kinetics of basaltic magmas. Front. Earth. Sci. 7:250. doi:

709   10.3389/feart.2019.00250

710   Vetere, F., Iezzi, G., Behrens, H., Holtz, F., Ventura, G., Misiti, V., Cavallo, A., Mollo, S.,

711   Dietrich, M., 2015. Glass forming ability and crystallisation behaviour of subalkaline

712   silicate   melts.   Earth-Sci.   Rev.   150,   25–44.

713   https://doi.org/10.1016/j.earscirev.2015.07.001

714 Vo, N. T., Atwood, R. C., Drakopoulos, M., 2018. Superior techniques for eliminating ring

715 artifacts in X-ray micro-tomography. Opt. Express. 26, 28396–28412.

716 https://doi.org/10.1364/OE.26.028396

717 Vo, N. T., Drakopoulos, M., Atwood, R. C., Reinhard, C., 2014. Reliable method for

718 calculating the center of rotation in parallel-beam tomography. Opt. Express 22,

719 19078–19086. https://doi.org/10.1364/OE.22.019078

720 Vona, A., Romano, C., 2013. The effect of undercooling and deformation on the

721 crystallization kinetics of Stromboli and Etna basalts. Contrib. Mineral. Petrol. 166,

722 491–509. https://doi.org/10.1007/s00410-013-0887-0

723 Vona, A., Romano, C., Dingwell, D. B., Giordano, D., 2011. The rheology of crystal-bearing

724 magmas. Geoch. Cosmoch. Acta. 75, 3214–3236.

725 https://doi.org/10.1016/j.gca.2011.03.031

726 Wentworth, C. K., Macdonald, G. A., 1953. Structures and forms of basaltic rocks in Hawaii.

727 U. S. Geological Survey Bulletin 994, 1–98. https://doi.org/10.3133/b994

728 Witter, J.B., Harris, A.J.L., 2007. Field measurements of heat loss from skylights and lava

729 tube systems. J. Geophys. Res. 112, B01203. https://doi.org/10.1029/2005JB003800

Figure 1 - Revised

Figure 1. Sketch of the experimental setup and *in situ* resistance furnace

Water-cooled stainless steel enclosure	Sample isolator (pyrophyllite)	Heating element
Heating connections	Sample isolator (Al_2O_3)	Thermocouples
Porous ceramic (Al_2O_3+SiO_2)	Rotating sample holder (Al_2O_3)	Magma sample

Figure 2

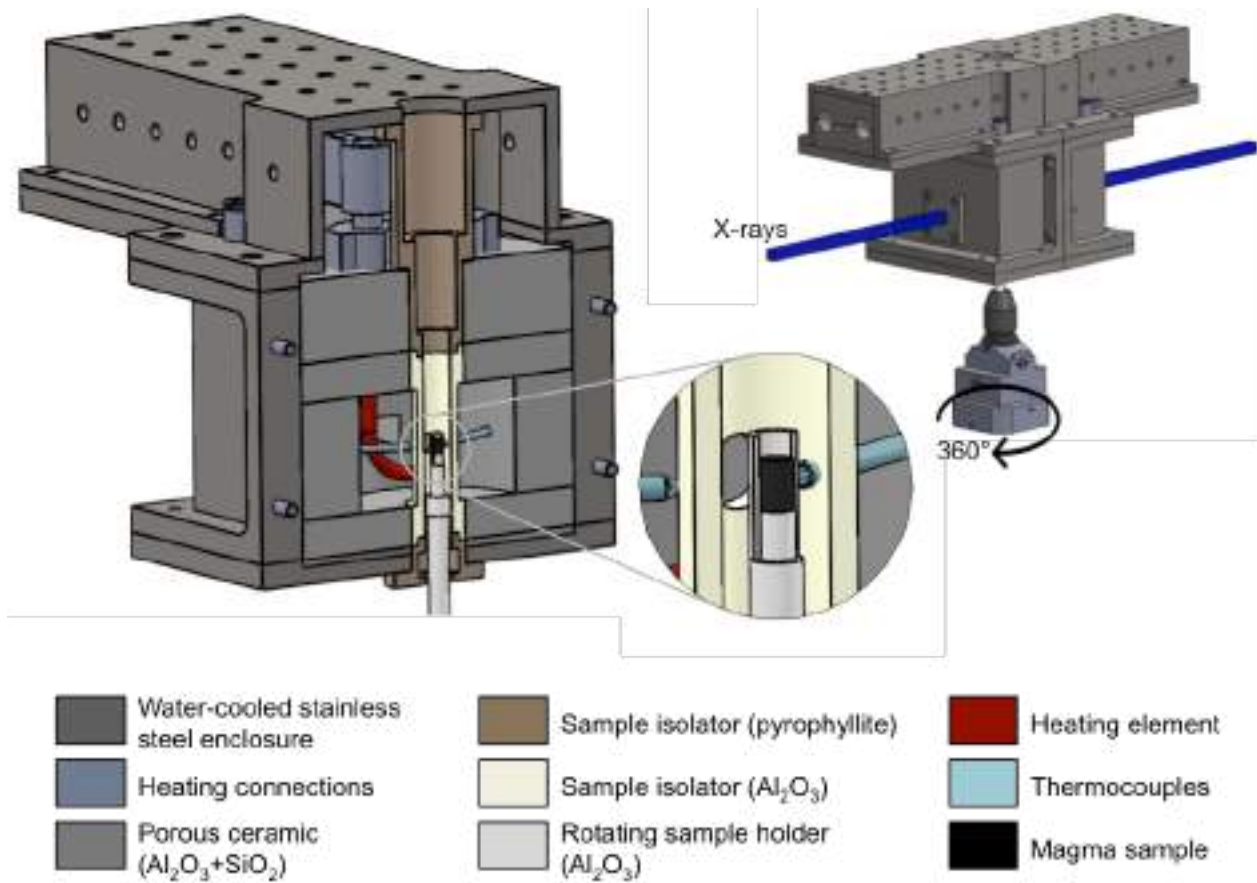Click here to access/download;Figure;Figure 2.pdf ±

Figure 2. Temperature-time paths followed by the three charges (SSC1170, SSC1150, CC0.5) of this study. t_0: start of the dwell time/cooling, t_1 = 60 min dwell/cooling, t_2 = 160 min dwell/cooling and t_3 = 200 min dwell/cooling. The small (± 5–10 °C) temperature fluctuations are due to sample rotation during image acquisition.
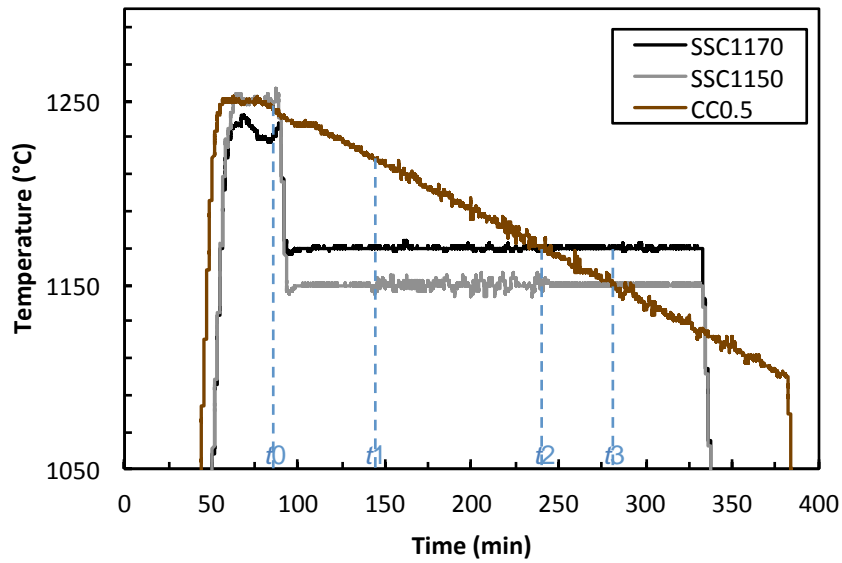
Figure 3

Figure 3. 3D volume renderings of charges SSC1170 (a–c), SSC1150 (d–f) and CC0.5 (g–i) through time, at t_1 = 60 min (a, d, g), t_2 = 160 min (b, e, h) and t_3 = 200 min (c, f, i) after the start of the dwell/cooling time (t_0). In each volume rendering, an orthoslice of the unsegmented dataset is shown in addition to segmented clinopyroxene (Cpx, in light blue) and plagioclase (Plg, in yellow) crystals. The volume fraction of crystals is given in %. Ox: Fe–Ti oxides.

Figure 4

Click here to access/download;Figure;Figure 4.pdf ⬇

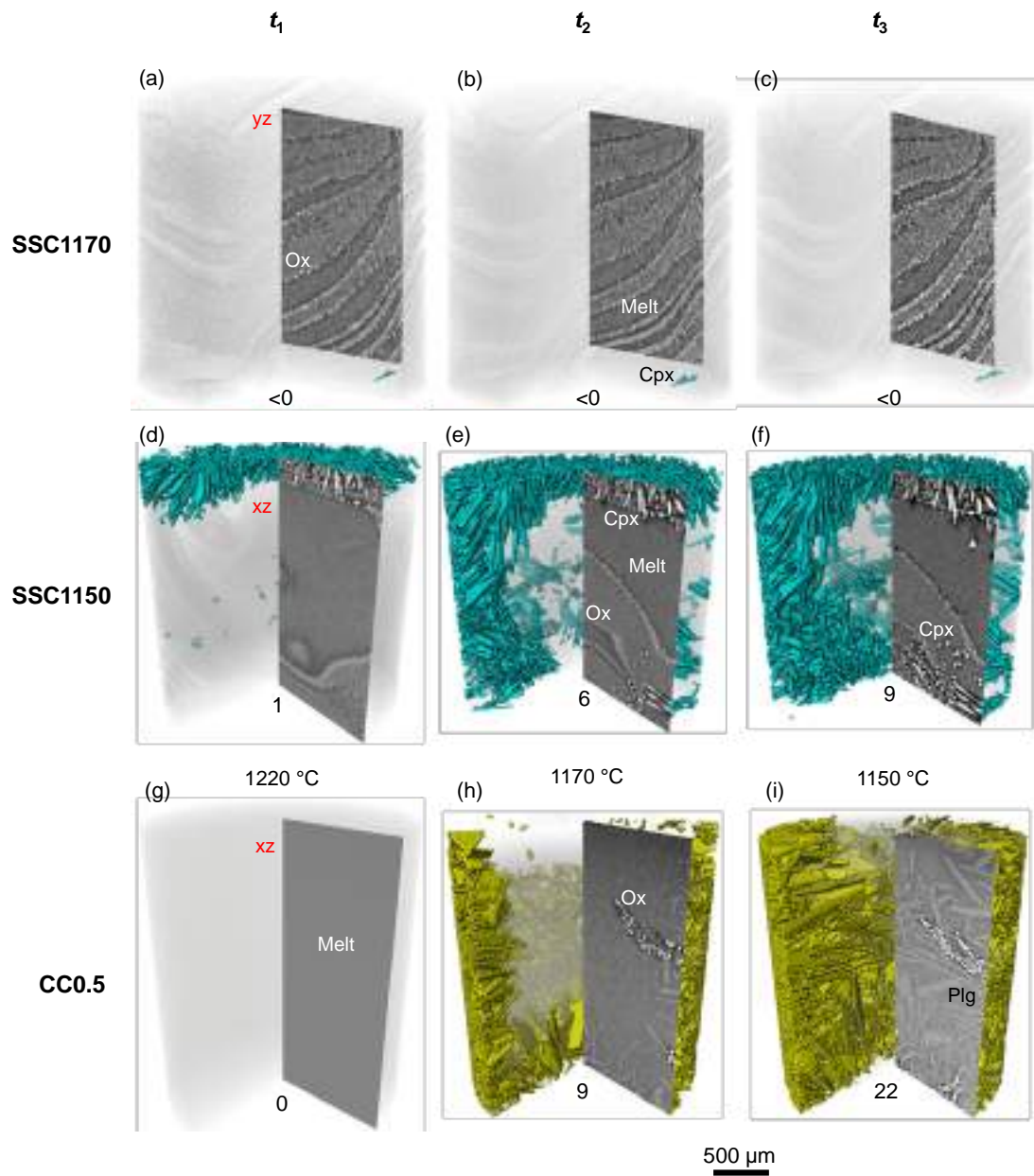**Figure 4.** Evolution of (a) clinopyroxene and (b) plagioclase sizes (3D crystal length L_{3D} and volume V) as a function of time and temperature in charges SSC1150 and CC0.5, respectively; t_1, t_2, $t_3 = 60$, 160, and 200 min dwell/cooling time, respectively. Error bars correspond to the standard deviation of the 3D crystal length/volume of the 10 crystals measured in each sample.

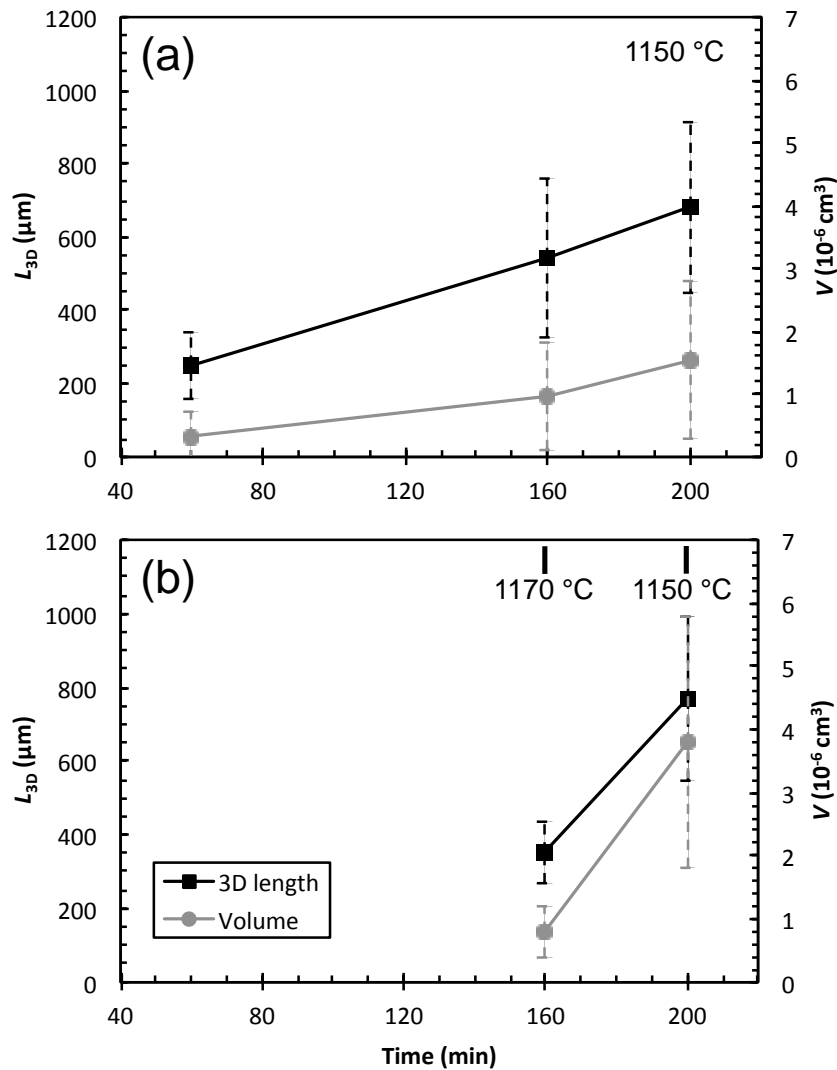Figure 5

Figure 5. Evolution of crystal growth rates (Y_{L3D} and Y_V) as a function of time and undercooling (ΔT); t_1, t_2, $t_3 = 60$, 160, and 200 min dwell/cooling time, respectively. Cpx: clinopyroxene crystals in SSC1150; Plg: plagioclase crystals in CC0.5. Error bars represent the standard deviation of the 10 crystals measured in each charge at t_1, t_2 and t_3.
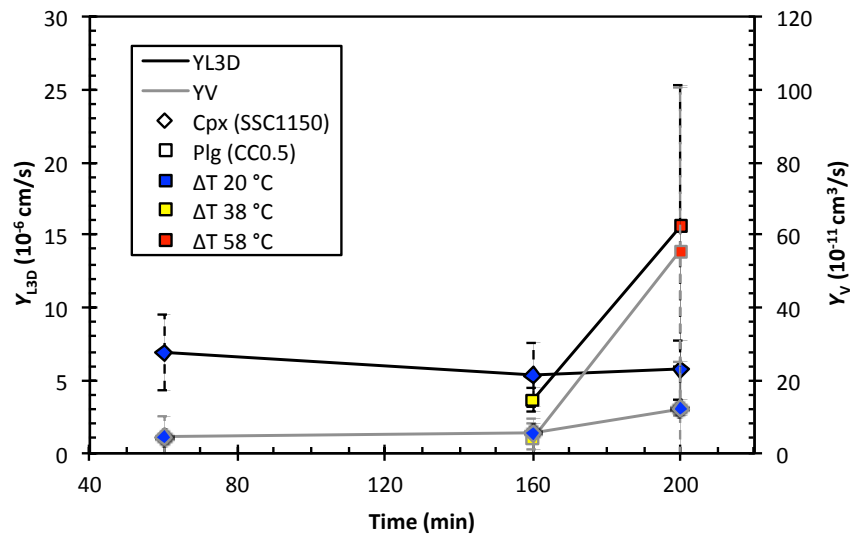
Figure 6 - Revised

Figure 6. Experimental vs. natural crystal compositons. Data from experiments SSC1170, SSC1150 and CC0.5. Natural data from Corsaro et al. (2007). Mg# (atomic Mg / (Mg + Fe^{2+})) in clinopyroxene crystals; Anorthite content ($100 \times$ atomic Ca / (Ca + Na)) in plagioclase crystals.
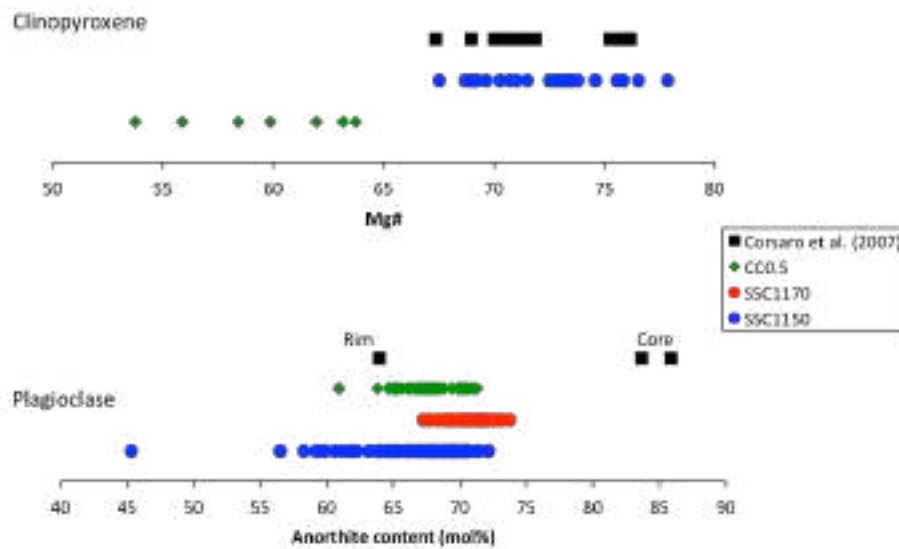
Table 1

Table 1. Composition of ET01 Lower Vents (LV) volcanics and starting glass, and of phenocrysts

Label	ET01[a] ($n = 6$)	Glass[b] ($n = 23$)	Cpx[c] ($n = 4$)	Plg[c] ($n = 3$)
SiO_2	47.7 (3)[d]	48.4 (2)	48.7 (17)	48.5 (34)
TiO_2	1.64 (2)	1.79 (7)	1.36 (48)	0.09
Al_2O_3	16.7 (1)	16.2 (5)	4.87 (119)	33.3 (22)
Fe_2O_3	1.77 (2)	nd	nd	nd
FeO	8.84 (11)	10.7 (3)	8.57 (35)	0.62 (15)
MnO	0.17 (0)	0.20 (3)	0.24 (5)	0.02
MgO	6.35 (16)	6.20 (32)	13.2 (11)	0.06 (1)
CaO	11.0 (1)	10.7 (2)	22.0 (7)	15.6 (26)
Na_2O	3.37 (6)	3.41 (20)	0.48 (9)	2.45 (1.30)
K_2O	1.89 (5)	1.90 (7)	nd	0.15 (19)
P_2O_5	0.48 (1)	0.54 (4)	nd	nd
Total	99.2	99.85	99.2	100.8

[a]Whole-rock composition (averaged and normalized to 100% anhydrous) of 2001 Lower Vents (LV) lava flow products, from Corsaro et al. (2007).
[b]Electron microprobe analysis (normalized to 100% anhydrous) of ET01 starting glass, from Arzilli et al. (2019). All Fe reported as FeO.
[c]Electron microprobe analyses of clinopyroxene (Cpx) and plagioclase (Plg) phenocrysts in 2001 LV volcanics, from Corsaro et al. (2007). All Fe reported as FeO.
[d]One standard deviation in terms of last digit unit cited.
n: number of analyses.
nd: not determined.
Oxides are in wt%.

Table 2   Click here to access/download;Table;Table 2.pdf

Table 2. Experimental conditions and results

| Charge	T_{init} (°C)	T_{exp} (°C)	R (°C/min)	dwell time (min)	ΔT (°C)	Phase assemblage[a]	L_{3D} (cm)	V (cm^3)	Y_{L3D} (cm/s)	Y_V (cm^3/s)
Single-step cooling (SSC)										
SSC1170	1250	1170	24	240	0	gl(92)+ox(8)+cpx(<0.1)	–	–	–	–
SSC1150	1250	1150	24	240	20	gl(83)+ox(8)+cpx(9)	6.8E–02 (2)	1.6E–06 (1)[b]	5.8E–06 (2)	1.2E–10 (1)
Continuous cooling (CC)										
CC0.5	1250	1100	0.5	–	≤108	gl(77)+plg(22)+ox(0.8)	7.7E–02 (2)	3.8E–06 (2)	1.6E–05 (1)	5.5E–10 (5)

Note: T_{init} = initial (or melting) temperature; T_{exp} = experimental (or final) temperature; R = cooling rate; ΔT = undercooling degree, $T_{liquidus} - T_{experimental}$ with $T_{liquidus}$ = 1208 °C for plagioclase and $T_{liquidus}$ = 1170 °C for clinopyroxene; L_{3D} = crystal length; V = crystal volume; Y_{L3D} = crystal growth rate = L_{3D}/t_{exp} with t_{exp} the experimental duration (in s, Arzilli et al., 2015); Y_V = volumetric growth rate = $(V \times 0.5)/t_{exp}$ (Arzilli et al., 2015); r_p = crystal length/width aspect ratio; ϕ_m = maximum crystal packing fraction; ϕ/ϕ_m = ratio of the crystal volume fraction to the maximum crystal packing fraction, κ = consistency; n = flow index. All textural parameters are averaged over 10 selected crystals at t_3 (after 200 min of dwell/cooling).
[a]Phase proportions calculated by 3D image analysis at t_3; gl, glass; cpx, clinopyroxene; plg, plagioclase; ox, Fe–Ti oxide. In SSC1150, the oxide contents were calculated to be 4 vol% and 8 vol% at t_1 and t_2, respectively.
[b]Standard deviation of the mean value.

Charge	r_p	ϕ_m	ϕ/ϕ_m	κ	n
Single-step cooling (SSC)					
SSC1170	–	–	–	–	–
SSC1150	7.35 (3)	0.38	0.24	1.72	1
Continuous cooling (CC)					
CC0.5	5.76 (2)	0.41	0.53	4.60	0.91

Fig. A.1. Longitudinal (XZ) slices through the 3D volume renderings of charges (a) CC0.5, (b) SSC1150 and (c) SSC1170 showing the heterogeneous nucleation of crystals (Plg: plagioclase, Cpx: clinopyroxene) after 60 min of cooling/dwell (t_1). Ox: oxide. The volume of interest (VoI, red inset) selected for quantitative image analysis is depicted in (a). In (c) a transverse (XY) slice of the SSC1170 charge is also depicted.
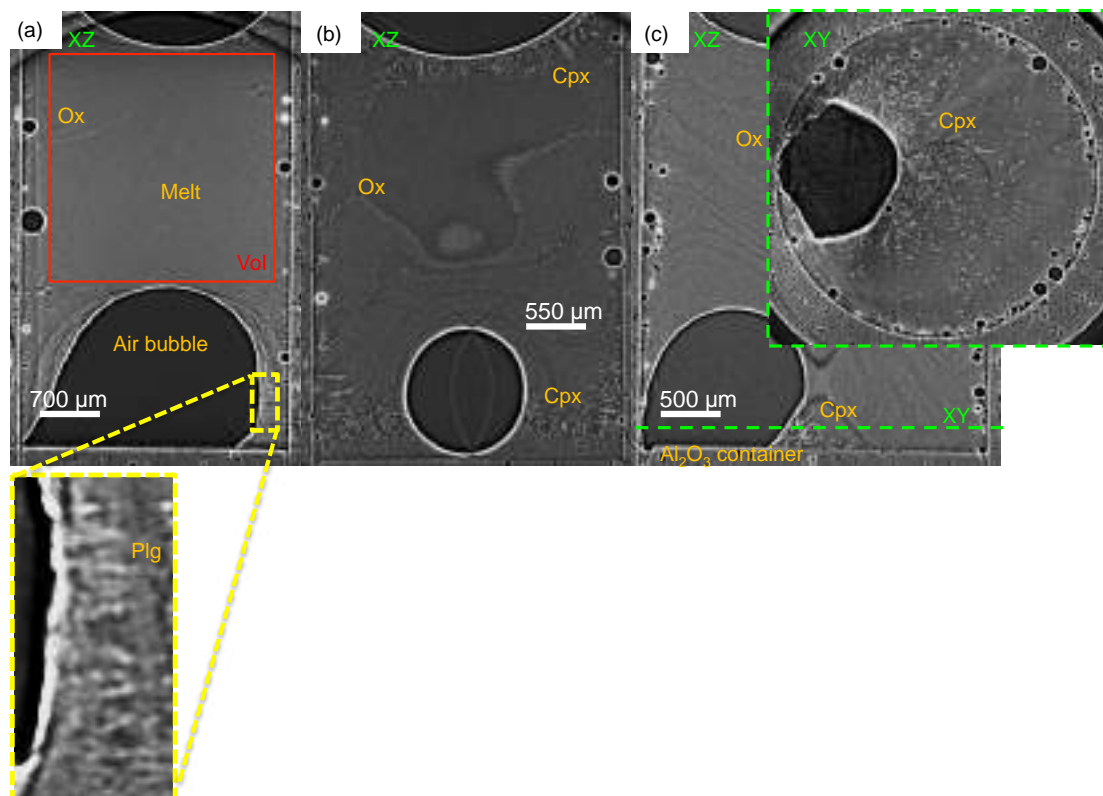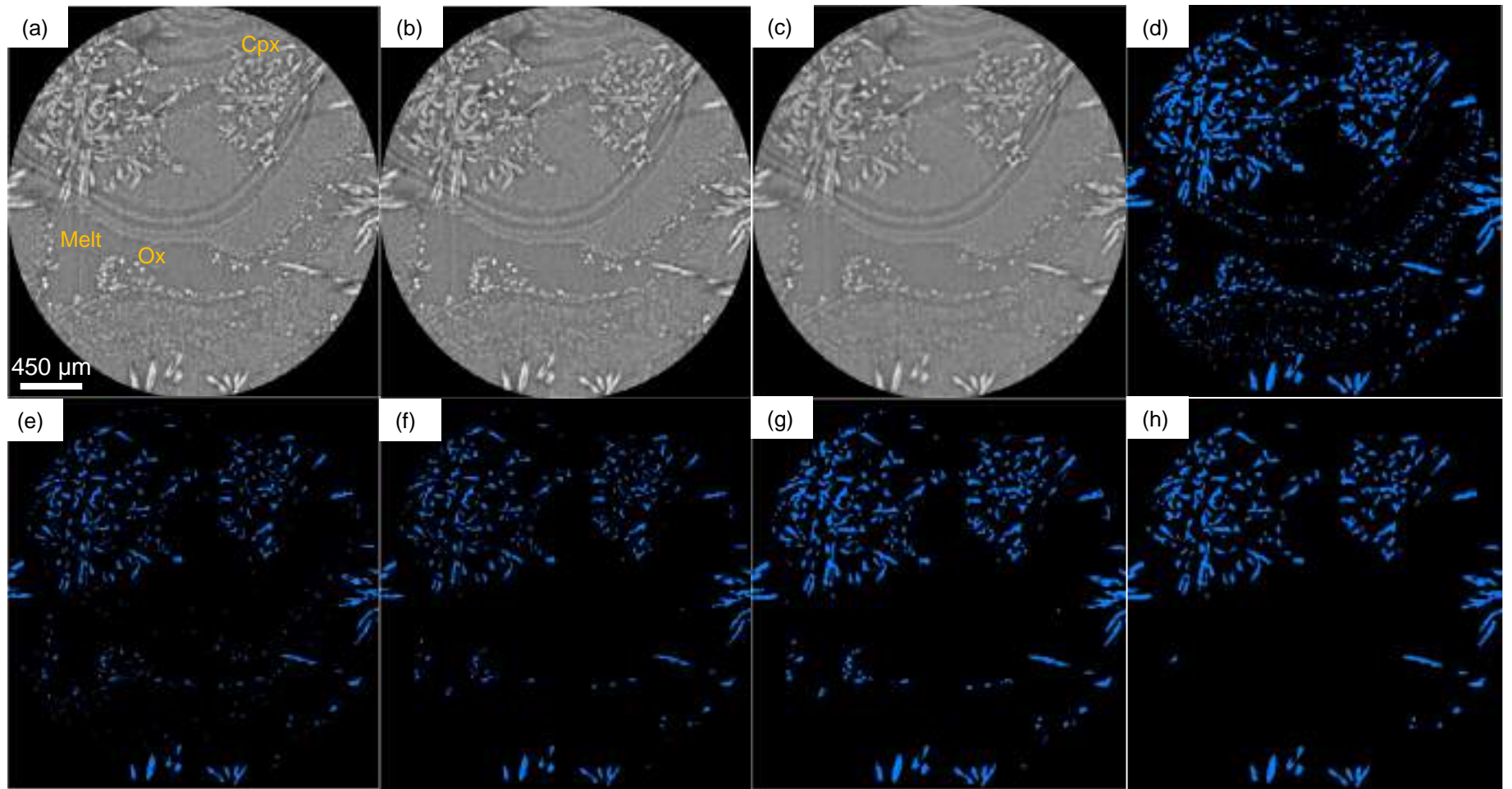
Fig. A.2. Overview of the image analysis procedure using Avizo. A transverse (XY) slice through the 3D volume rendering of the SSC1150 charge after 160 min of dwell (t_2) is shown for illustration. (a) Initial stage, after pre-processing with ImageJ; (b) After bilateral filtering; (c) After median filtering; (d) After interactive thresholding; (e) After erosion; (f) After removing small spots; (g) After dilation; (h) Final stage, after manual correction. Cpx: clinopyroxene; Ox: oxide.

Fig. A.3. Selected clinopyroxene (a) and plagioclase (b) crystals in samples SC1150 and CC0.5, respectively. Scale bars: 200 μm.

Fig. A.4. (a) SEM image of a test sample showing the formation of an oxide layer on the edge of an alumina container. The sample is a basalt from the Mt. Etna eruption of 2001 that has been le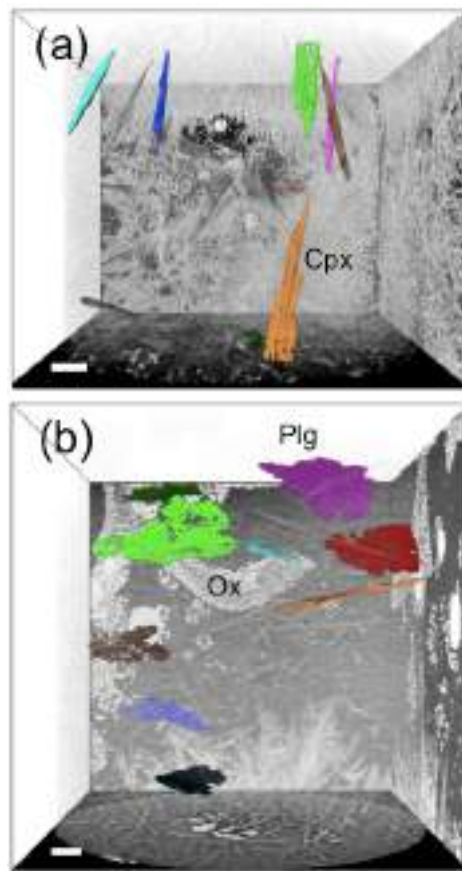ft 5 hours in air, at 1 atm and 1190 °C before being air-quenched. (b) ESD analyses demonstrating that the oxides are made of Al and Mg. Ox: oxide; plg: plagioclase; cpx: clinopyroxene.
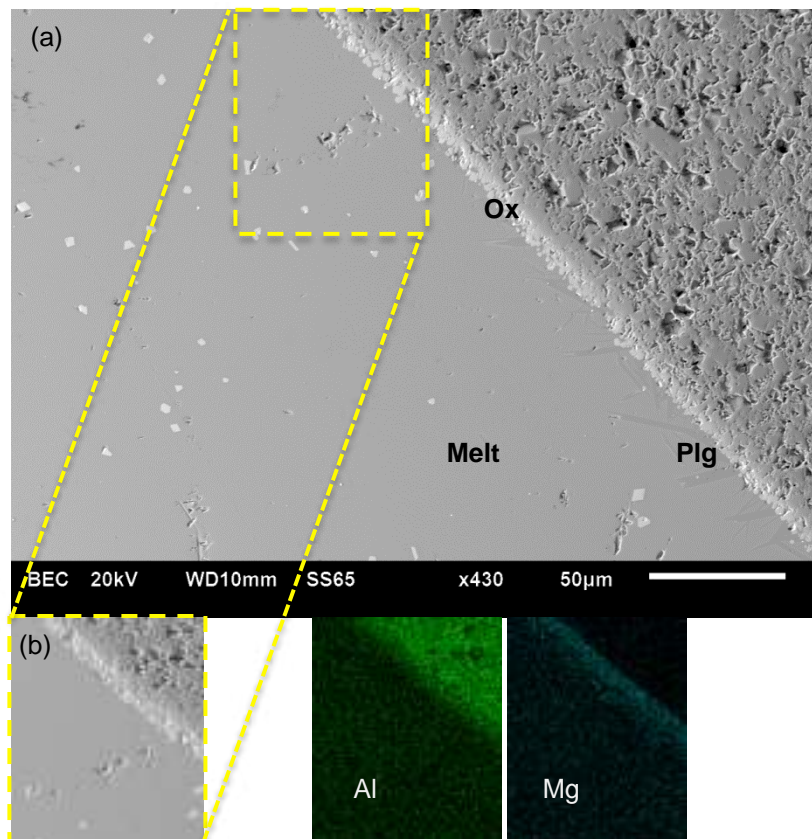
Table A.1. Experimental compositions

Charge	Phase	SiO_2	TiO_2	Al_2O_3	FeO	MnO	MgO	CaO	Na_2O	K_2O	P_2O_5	Cr_2O_3	NiO	Total	Mol%
SSC1170	gl[a](3)[b]	50.6(4) [c]	1.85(6)	15.8(1)	8.52(11)	0.22(4)	6.25(1)	11.3(2)	3.41(9)	1.50(16)	0.52(7)	0.03(1)	0.03(1)	98.0	
SSC1150	gl(10)	53.4(4)	1.73(3)	18.1(2)	5.90(16)	0.18(1)	4.77(16)	7.97(24)	4.91(7)	2.84(10)	nd	0.01(0)	0.01(0)	96.2	
	cpx(26)	42.7(12)	1.88(29)	7.97(86)	9.21(69)	0.17(2)	13.3(8)	21.0(3)	0.47(3)	0.01(1)	nd	0.01(1)	0.01(1)	96.8	$En_{45}Wo_{40}$
CC0.5	gl(8)	53.8(12)	2.11(20)	14.9(7)	7.13(88)	0.24(8)	5.37(56)	7.57(67)	4.49(58)	3.53(40)	0.85(17)	0.02(1)	0.02(0)	98.2	
	plg(69)	51.1(8)	0.14(4)	27.6(6)	2.99(28)	0.03(2)	0.22(10)	13.4(4)	3.49(24)	0.41(7)	0.05(5)	0.02(1)	0.02(1)	99.3	$An_{68}Or_7$

[a]Glass analyses normalized to 100% anhydrous, with all Fe as FeO.
[b]Number of microprobe analyses.
[c]One standard deviation in terms of last digit unit cited.
n: number of analyses.
nd: not determined.
gl, glass; cpx, clinopyroxene; plg, plagioclase. Enstatite En = 100 × at. Mg / (Mg + Fe + Ca); Wollastonite Wo = 100 × at. Ca / (Mg + Fe + Ca) in pyroxene, calculated with Fe = FeO; Anorthite An = 100 × at. Ca / (Ca + Na); Orthoclase Or = 100 × at. K / (K + Na) in plagioclase.

Table A.2. 3D clinopyroxene crystal measurements

Crystal	Time	L_{3D} (cm)	Y_{L3D} (cm/s)	V (cm^3)	Y_V (cm^3/s)	r_p
cpx-01	t_1	0.032	9.0E-06	1.0E-06	1.4E-10	2.22
	t_2	0.063	5.1E-06	2.7E-06	1.4E-10	3.58
	t_3	0.069	2.4E-06	2.9E-06	3.0E-11	3.61
cpx-02	t_1	0.032	8.8E-06	2.4E-07	3.4E-11	5.31
	t_2	0.074	7.0E-06	9.5E-07	5.9E-11	12.6
	t_3	0.087	5.4E-06	1.5E-06	1.1E-10	11.1
cpx-03	t_1	0.026	7.2E-06	2.5E-07	3.5E-11	5.69
	t_2	0.049	3.8E-06	6.3E-07	3.1E-11	7.08
	t_3	0.071	9.2E-06	9.7E-07	7.2E-11	7.89
cpx-04	t_1	0.026	7.1E-06	1.2E-07	1.6E-11	–
	t_2	0.068	7.1E-06	6.4E-07	4.4E-11	14
	t_3	0.079	4.4E-06	9.7E-07	6.9E-11	12.4
cpx-05	t_1	0.009	2.5E-06	4.1E-08	5.8E-12	3.05
	t_2	0.036	4.4E-06	5.2E-07	4.0E-11	4.26
	t_3	0.05	6.1E-06	1.0E-06	1.1E-10	4.99
cpx-06	t_1	–	–	–	–	–
	t_2	0.089	9.2E-06	2.3E-06	1.2E-10	5.54
	t_3	0.109	8.4E-06	4.6E-06	4.9E-10	6.03
cpx-07	t_1	–	–	–	–	–
	t_2	0.062	6.5E-06	6.4E-07	3.3E-11	10.1
	t_3	0.079	6.9E-06	1.1E-06	1.1E-10	11
cpx-08	t_1	–	–	–	–	–
	t_2	0.055	5.7E-06	8.9E-07	4.7E-11	7.19
	t_3	0.064	4.0E-06	1.2E-06	7.3E-11	7.36
cpx-09	t_1	–	–	–	–	–
	t_2	0.032	3.3E-06	2.7E-07	1.4E-11	5.75
	t_3	0.047	6.3E-06	7.7E-07	1.0E-10	5.88
cpx-10	t_1	–	–	–	–	–
	t_2	0.015	1.5E-06	9.5E-08	5.0E-12	3.97
	t_3	0.025	4.4E-06	4.3E-07	7.0E-11	3.24

cpx, clinopyroxene; L_{3D} = 3D crystal length; Y_{L3D} = crystal growth rate; V = crystal volume; Y_V = volumetric crystal growth rate; r_p = crystal aspect ratio (= length/width ratio). t_1, t_2, t_3 = 60, 160, and 200 min dwell, respectively.

Note that at t_2 growth rates are calculated for the time interval between t_1 and t_2 and at t_3 the rates are calculated for the t_2–t_3 time interval.

These single measurements are assumed to contain an error of 10% because of variation in the segmentation threshold.

Table A.3. 3D plagioclase crystal measurements

Crystal	Time	L_{3D} (cm)	Y_{L3D} (cm/s)	V (cm^3)	Y_V (cm^3/s)	r_p
plg-01	t_2	0.052	5.4E-06	1.3E-06	6.7E-11	4.40
	t_3	0.101	2.0E-05	6.2E-06	1.0E-09	4.36
plg-02	t_2	0.045	4.7E-06	1.6E-06	8.2E-11	4.90
	t_3	0.058	5.5E-06	2.8E-06	2.6E-10	6.21
plg-03	t_2	0.038	4.0E-06	1.0E-06	5.2E-11	3.71
	t_3	0.070	1.3E-05	2.9E-06	4.0E-10	4.20
plg-04	t_2	0.035	3.7E-06	6.0E-07	3.1E-11	3.98
	t_3	0.065	1.2E-05	2.5E-06	3.9E-10	4.64
plg-05	t_2	0.034	3.6E-06	9.6E-07	5.0E-11	4.17
	t_3	0.059	1.0E-05	2.3E-06	2.8E-10	5.10
plg-06	t_2	0.031	3.2E-06	3.4E-07	1.8E-11	6.08
	t_3	0.090	2.5E-05	3.9E-06	7.5E-10	9.63
plg-07	t_2	0.028	2.9E-06	5.8E-07	3.0E-11	3.90
	t_3	0.045	6.9E-06	1.5E-06	1.9E-10	3.87
plg-08	t_2	0.028	2.9E-06	4.1E-07	2.1E-11	3.49
	t_3	0.116	3.7E-05	8.1E-06	1.6E-09	6.45
plg-09	t_2	0.027	2.8E-06	4.0E-07	2.1E-11	3.49
	t_3	0.072	1.9E-05	2.6E-06	4.5E-10	9.11
plg-10	t_2	–	–	–	–	–
	t_3	0.095	8.0E-06	4.9E-06	2.0E-10	3.98

plg, plagioclase; L_{3D} = 3D crystal length; Y_{L3D} = crystal growth rate; V = crystal volume; Y_V = volumetric crystal growth rate; r_p = crystal aspect ratio (= length/width ratio). t_1, t_2, t_3 = 60, 160, and 200 min cooling time, respectively.

Note that at t_2 growth rates are calculated for the time interval between t_1 and t_2 and at t_3 the rates are calculated for the t_2–t_3 time interval.

These single measurements are assumed to contain an error of 10% because of variation in the segmentation threshold.

Credit Author Statement

M.P., M.R.B., F.A. and P.D.L. conceived the research project. All authors, N.L.G., F.A., G.L.S., M.P., B.C., M.E.H., N.T.V., R.C.A., D.D.G., S.N., E.W.L., M.R.B. and P.D.L. contributed to the beamline experiments. F.A. collected the volcanic rocks for the starting material. D.D.G. prepared the starting material. F.A., M.P., G.L.S. and N.T.V. performed image reconstruction. N.L.G. performed image processing with help from F.A. and M.P. N.LG. performed the image segmentation and analysis. F.A. and M.E.H. performed chemical analysis. N.L.G. wrote the manuscript, with contributions from all other authors.